

Supplementary Materials for

**Topological magnon insulators in two-dimensional van der Waals
ferromagnets CrSiTe₃ and CrGeTe₃: Toward intrinsic gap-tunability**

Fengfeng Zhu*, Lichuan Zhang, Xiao Wang, Flaviano José dos Santos, Junda Song, Thomas Mueller,
Karin Schmalzl, Wolfgang F. Schmidt, Alexandre Ivanov, Jitae T. Park, Jianhui Xu, Jie Ma,
Samir Lounis, Stefan Blügel, Yuriy Mokrousov*, Yixi Su*, Thomas Brückel

*Corresponding author. Email: f.zhu@fz-juelich.de (F.Z.);
y.mokrousov@fz-juelich.de (Y.M.); y.su@fz-juelich.de (Y.S.)

Published 10 September 2021, *Sci. Adv.* 7, eabi7532 (2021)
DOI: 10.1126/sciadv.abi7532

This PDF file includes:

Sections S1 to S3
Figs. S1 to S11

1 DATA ANALYSIS

1.1 X-ray diffraction, magnetic properties and neutron scattering

The lattice parameter $c = 20.681(75)$ Å for CrSiTe₃ and $c = 20.603(99)$ Å for CrGeTe₃ at room temperature extracted from XRD (in Fig.S1[(a),(b)]) is quite consistent with the previous results (52–54). From the temperature dependence of the magnetic susceptibility (shown in Fig.S1[(c),(d)]), the ferromagnetic transitions can clearly be observed at $T_c \approx 33$ K for CrSiTe₃ and $T_c \approx 63$ K for CrGeTe₃, respectively. In the insets of Fig.S1[(c),(d)], the isothermal magnetization ($M - H$) curves show small magnetic anisotropies, and the magneto-crystalline anisotropy is extracted as 0.09 meV for CrSiTe₃ and 0.02 meV for CrGeTe₃, respectively. In Fig.S1[(e),(f)], the phase transition is also observed from the temperature dependence of the (1,1,0) magnetic Bragg peak for both CrSiTe₃ and CrGeTe₃. The temperature dependence of the order parameter were fitted with the power law equation $I = I_0 + A(1 - \frac{T}{T_N})^{2\beta}$, the fitted transition temperatures are about 33 K for CrSiTe₃ and 63 K for CrGeTe₃, which are in a good agreement with our magnetization results. The critical exponents are extracted as $\beta = 0.151(3)$ for CrSiTe₃ and $\beta = 0.201(7)$ for CrGeTe₃.

With polarized neutron diffraction, we can easily determine the directions of the ordered magnetic moments, because the sign of polarized neutrons can only be flipped when there exists a non-zero component of magnetic moments perpendicular to the polarization of the neutron beam \mathbf{P} and the scattering wave vector \mathbf{Q} . Due to a favorable situation related to the

ferromagnetic domains in this sample, no neutron depolarization was noticed for the polarized measurements in the ferromagnetic state. As shown in Fig.S2, 2D Q-maps in the (H,K,0) and (H,H,L) planes of reciprocal space at three different polarization modes were measured at 4 K. The diffraction patterns of x and y polarization for the respective spin-flip and non-spin-flip channels (Fig.S2(a-d)) are basically the same in the (H,K,0) scattering plane, and all the nuclear and magnetic diffraction peaks relocated on the same position in the center of Brillouin zone, which indicates its ferromagnetic character and that the ferromagnetic moment has a non-zero component along the z directions at least. For the z polarization, there are no diffraction peaks observed in the spin-flip channel but the same diffraction pattern as in the previous xy polarizations of the non-spin-flip channel, as shown in Fig.S2[(e),(f)], which confirms that the ordered ferromagnetic moments are aligned exclusively along the c axis. The absence of the $(0,0,3n)$ magnetic reflections in the x spin-flip channel compared to the x non-spin-flip channel (shown in Fig.S2(g)), also indicates the magnetic moments are aligned along the c axis.

For the measurements of spin-wave excitations, the full width at half maximum of CrSiTe₃ is much smaller than that of CrGeTe₃. For CrSiTe₃ single crystals, due to the large size and thickness, we used only 2 single crystals and the FWHM of the co-aligned sample turns out to be only 1.4° in the rocking curve scan at IN8, as shown in Fig.S3(a). However, for CrGeTe₃ single crystals, their usual dimension is about 2 mm × 2 mm × 0.5 mm, so we co-aligned about 0.8 g samples on 5 horizontal aluminum plates and about 0.6 g samples on 3 vertical aluminum plates for the experiments with (H,K,0) and (H,H,L) as scattering planes, respectively. The corresponding FWHM of the (H,K,0) orientated CrGeTe₃ sample is about 3.52° (shown in Fig.S3(b)).

1.2 Constant-energy mapping around the K points

To gain more information about the the magnon band dispersion in the vicinity of the K points, we have also very carefully measured the constant-energy scan contour maps in the (H,K,0)

reciprocal plane with various energy transfers, as shown in Fig.S4(a-h). The energy transfers were selected from 7.5 meV to 11 meV with a step of 0.5 meV to cover the whole range of the gap opening at the K points. In Fig.S4(q), a 2D reciprocal space map with BZ boundaries and high-symmetry points in (H,K,0) is shown, and the measured regions of the constant-energy slices in Q space are indicated by the light blue hexagons. However, the spectral function (or dynamic structure factor) is strongly dependent on the momentum transfer, causing intensity enhancement or suppression in some specific parts of the contour maps. According to the previously calculated spectral function for the honeycomb ferromagnet with DM interactions, the magnon shows a shorter lifetime in the acoustic mode on one side of the K point and, in the optical mode on the opposite side of K , which is consistent with the antisymmetric intensity distribution that we observed in Fig.S4(a-h). From the constant-energy slices, the 2D projected magnon “cone” is observed to become weaker and smaller towards the gap energy, and become larger again by increasing energy transfers. In between, for example at $E = 9.5$ meV, only discrete spots with weak intensity can be seen at the K points, as shown in Fig.S4(e).

Although the existence of a gap opening is almost clear by observing the intensity change of the constant-energy contours, it is not rigorous and convincing enough, given that similar constant-energy contours were also observed in the topological Dirac magnon material CoTiO_3 where there exists no gap at the K points (17). To exclude the involvement of the Dirac magnon, further detailed constant- Q energy scans at various K points are quite necessary. In Fig.S4(r), the energy-scan line profiles were extracted at three K points [highlighted by green circles in Fig.S4(q)] with different momentum transfers, and all of them show two peaks located at around 8.7 meV and 10.7 meV, which clearly indicate a 2 meV gap opening at around 9.5 meV. Due to the limited energy resolution of ~ 1.3 meV that is also comparable to the gap size, the in-gap intensity is not exactly zero in our experimental configuration. By applying a convolution of the instrument energy resolution, similar constant-energy patterns including the discrete spot-

shaped contours at $E = 9.5$ meV can be very well reproduced in our simulations, as shown in Fig.S4(i-p).

1.3 Determination of the magnon gap at the Brillouin zone center

We tried to measure the spin wave gap at the Γ point by using one of the best cold neutron triple-axis spectrometers, IN12, but we failed although the energy resolution and background level were quite good. Unlike CrI_3 , the anisotropy in both CrSiTe_3 and CrGeTe_3 is very small (32, 34, 35), it is really hard to resolve it directly from our low energy scan data. To give out a reference value of the spin wave gap, we carefully measured the low energy magnon bands along the high-symmetry directions at 2 K. In the color map of Fig.S5(a), the magnon bands of CrGeTe_3 below 15 meV were measured at IN12 with $k_f = 1.7 \text{ \AA}^{-1}$, and the magnon bands above 15 meV were measured with $k_f = 2.8 \text{ \AA}^{-1}$. Fig.S5(b) shows the corresponding calculated dispersion curves of the same Q path as in Fig.S5(a) by using the fitted exchange parameters in the Heisenberg-DM model. In the vicinity of the Γ point at low energy, the magnon bands dispersions along $\Gamma - M$ and $\Gamma - K$ can be both fitted by the parabolic equation under the long-wave approximation. Here, for the quadratic fitting, the Gauss fitted peak positions of the measured magnon bands below 5 meV were included, as shown in the red rectangular frame of Fig.S5(c). The fitting results were shown in the form of the energy as a linear function of the squared moment transfer Q , and the fitted gap size at the Γ point is about 0.0097 meV but with a very large error of 0.183 meV, which indicates the gap of CrGeTe_3 is rather small and really hard to resolve by triple-axis spectroscopy.

For the same reason, the magnon band dispersions of CrSiTe_3 and CrGeTe_3 along the $[0 0 L]$ direction were also fitted to gain a reference value of the spin wave gap at the Γ point, as shown in Fig.S6. Given the magnetic structure is ferromagnetic in both the intralayers and also the vdW interlayers, we can treat every three ABC-stacked ferromagnetic Cr^{3+} as a single imaginary spin with $S = 3/2 \times 3$, so the spin wave dispersion along the c axis that is concerned

here can be approximately described by using a one-dimensional ferromagnetic model with an effective nearest-neighbor ferromagnetic exchange interaction \tilde{J} :

$$H = -\tilde{J} \sum_i (S_i^x S_{i+1}^x + S_i^y S_{i+1}^y + \Delta S_i^z S_{i+1}^z) - A_{zz} \sum_i (S_i^z)^2, \quad (\text{S1})$$

where Δ and A_{zz} denote the exchange and single-ion anisotropy, respectively. In the case $\Delta = 1$, the exchange interaction reduces to the isotropic Heisenberg interaction. At low temperatures ($k_B T \ll \tilde{J}$), the perturbations of the ground state are very small, so we can ignore the high-order terms and just keep the ground-state energy term and quadratic terms in bosonic operators. Finally, the ferromagnetic magnon dispersion can be written as

$$\epsilon_k = 2\tilde{J}S(\Delta - \cos(kc)) + 2A_{zz}S, \quad (\text{S2})$$

where c is the lattice constant along the z direction. The gap at the Brillouin zone center Γ point is expressed as $2\tilde{J}S(\Delta - 1) + 2A_{zz}S$. The band dispersions in Fig.S6 were fitted by using Eq.S2, and the effective exchange interactions \tilde{J} were determined as 0.11(1) and 0.16(2) meV for CrSiTe₃ and CrGeTe₃ respectively. From the fitting results, we failed to get the anisotropy gap size because of the extremely small magnetic anisotropy in CrXTe₃. To give an idea of how small the single-ion anisotropy is, we set $\Delta = 1$, namely Heisenberg interaction, and the single-ion anisotropy is estimated as $A_{zz} < 0.0018$ meV for CrSiTe₃ and $A_{zz} < 0.020$ meV for CrGeTe₃. The small single-ion anisotropy can basically be neglected, compared to the large in-plane exchange interactions J_{ab} . However, for the overall magnon band fitting (e.g. in Fig.S5(b)), we symbolically set the single-ion anisotropy A as 0.01 meV for the Hamiltonian in Eq.S1.

2 SPIN HAMILTONIAN

2.1 Heisenberg-DM model

For the CrXTe_3 , although the DM interaction will cancel because of the space inversion between the nearest-neighbor Cr atoms, the second nearest-neighbor interaction, the space inversion symmetry is actually broken in a honeycomb lattice, leading to a non-zero DM interaction. Although the Te atoms may appear to have the strongest SOC in CrXTe_3 , the magnitude of the DM interaction is more likely determined by the competition of one Cr atom and two Si/Ge atoms on two sides of the second nearest-neighbor Cr-Cr bond. Here we use LSWT to calculate the magnon spectra of CrXTe_3 , starting from the generalized Heisenberg model (40),

$$H = \sum_{i < j} \mathbf{S}_i^\dagger \hat{J}_{ij} \mathbf{S}_j, \quad (\text{S3})$$

where the interaction tensor between the lattice sites i and j

$$\hat{J}_{ij} = \begin{pmatrix} J_{ij}^x & D_{ij}^z & -D_{ij}^y \\ -D_{ij}^z & J_{ij}^y & D_{ij}^x \\ D_{ij}^y & -D_{ij}^x & J_{ij}^z \end{pmatrix} \quad (\text{S4})$$

includes the symmetric exchange \mathbf{J}_{ij} and the antisymmetric off-diagonal DM interaction terms \mathbf{D}_{ij} , caused by the spin-orbit coupling. The DM interaction vector is defined as $\mathbf{D}_{ij} = (D_{ij}^x, D_{ij}^y, D_{ij}^z)$. Based on the symmetry and the Moriya's rule, the direction of the DM interaction vector is determined as out of plane. Similar to earlier works (27), we include five Heisenberg exchange interactions in total, three in the intra-layers and two between the inter-layers, with their numerical values listed in Table .

According to the LSWT, the Holstein-Primakoff transformation (55) is adopted for the quantum spin operators. Followed by the Fourier transformation for the boson operators, the Hamiltonian matrix in momentum space is obtained. Then the eigenvalue and eigenvector, namely the magnon band dispersion can be extracted through diagonalizing the matrix. As we expected,

the band opens a gap at the K point which is consistent with our experimental results.

2.2 Heisenberg-Kitaev model

The Kitaev interaction is introduced to understand the magnetic behaviors that are close to quantum spin liquids in some $S=1/2$ honeycomb lattices with edge-sharing octahedra compounds, e.g., Na_2IrO_3 , $\alpha\text{-RuCl}_3$ (43,56). For the $S=3/2$ systems, like CrXTe_3 , the Kitaev-type exchange interaction may also exist, and recent theoretical works (57) have proposed to realize the Kitaev quantum spin liquid state in CrGeTe_3 by applying proper in-plane strain. As shown in the schematic of Fig.S7(a), the nearest Cr-Cr pairs are proposed to have three bond-dependent Ising exchange interactions in the local $\{\alpha\beta\gamma\}$ coordinate bases for the Kitaev model. For simplicity, here we first discuss the Kitaev model in the perfect orthogonal $\{\alpha\beta\gamma\}$ coordinate bases. The Heisenberg-Kitaev Hamiltonian can be expressed as:

$$H = - \sum_{i<j} J_{ij} \mathbf{S}_i \cdot \mathbf{S}_j - \sum_{\langle i,j \rangle_\nu} K^\nu S_i^\nu S_j^\nu - A_{zz} \sum_i (S_i^z)^2, \quad (\text{S5})$$

where the first term is the Heisenberg exchanges term and the second term represents the nearest neighbour bond-dependent Kitaev interaction with $K^\alpha=K^\beta=K^\gamma=K$. To obtain the final magnon dispersion, the Kitaev term in the Hamiltonian expressed by the local $\{\alpha\beta\gamma\}$ basis can be converted into the global $\{xyz\}$ coordinate in advance to apply the Holstein-Primakoff transformation and Fourier transformation, and then the total Hamiltonian can be rewrote in momentum space by bosonic operators. According to the linear-spin-wave theory, we can ignore the high-order terms and just keep the ground-state energy term and the linear terms which contain the magnon relation. By fitting the experimental results with the model, we can easily obtain the exchange parameters. Comparing to the previous Heisenberg-DM model, the DM term is just replaced by the Kitaev term, and also up to five isotropic Heisenberg interactions are included for CrXTe_3 . To make the calculated magnon bands consistent with the measured

band dispersion, the optimized Kitaev interaction parameters are quite large comparing to their nearest-neighbor Heisenberg interaction for both CrSiTe₃ and CrGeTe₃. The corresponding exchange parameters for CrXTe₃ are listed in Table.S1. As shown in Fig.S8, the magnon band of CrSiTe₃ reproduced by the Heisenberg-Kitaev model is quite similar to the result of the pure Heisenberg model but opens a gap in the vicinity of the K point like that of the Heisenberg-DM model.

However, it is important to realize that the $\{\alpha\beta\gamma\}$ basis is not perfectly orthogonal in CrXTe₃, the interangle between the local $\{\alpha\beta\gamma\}$ basis vectors is about 93.6° and 100.1° for CrSiTe₃ and CrGeTe₃ respectively. As shown in the schematic picture of Fig.S7(b), the local $\{\alpha\beta\gamma\}$ basis vectors tilt from the z axis towards the xy plane by an angle θ , and only when $\theta = \theta_0 \approx 54.74^\circ$, namely $\tan \theta = \sqrt{2}$, the $\{\alpha\beta\gamma\}$ basis becomes perfectly orthogonal (58). Here in our paper, we take θ as 57.28° and 62.26° from the experimental refined atomic structures of CrSiTe₃ and CrGeTe₃ respectively. The imperfection of θ will yield non-zero off-diagonal components when the exchange matrix is converted into the orthogonal $\{\alpha'\beta'\gamma'\}$ basis and eventually induce an extra exchange anisotropy along the global z axis. Three general Kitaev interaction matrices in a local $\{\alpha\beta\gamma\}$ basis can be expressed as:

$$\begin{pmatrix} K^\alpha & & \\ & 0 & \\ & & 0 \end{pmatrix}, \quad \begin{pmatrix} 0 & & \\ & K^\beta & \\ & & 0 \end{pmatrix}, \quad \begin{pmatrix} 0 & & \\ & 0 & \\ & & K^\gamma \end{pmatrix}, \quad (\text{S6})$$

and in the orthogonal $\{\alpha'\beta'\gamma'\}$ basis, they can be rewritten as:

$$\begin{pmatrix} A^2 & AB & AB \\ AB & B^2 & B^2 \\ AB & B^2 & B^2 \end{pmatrix} \cdot \frac{K^\alpha}{C^2}, \quad \begin{pmatrix} B^2 & AB & B^2 \\ AB & A^2 & AB \\ B^2 & AB & B^2 \end{pmatrix} \cdot \frac{K^\beta}{C^2}, \quad \begin{pmatrix} B^2 & B^2 & AB \\ B^2 & B^2 & AB \\ AB & AB & A^2 \end{pmatrix} \cdot \frac{K^\gamma}{C^2}, \quad (\text{S7})$$

where $A = 2 \sin \theta \cos \theta_0 + \cos \theta \sin \theta_0$, $B = -\sin(\theta - \theta_0)$ and $C = 3 \sin \theta_0 \cos \theta_0$. Especially when $\theta = \theta_0$, then we have $B = 0$ and $A = C$, the Eq.S7 is immediately degenerated into the simple form the same as the Eq.S6. However for CrSiTe₃ and CrGeTe₃ here, the off-diagonal

term is non-zero due to $\theta \neq \theta_0$, hence for example one of the Kitaev matrices will representatively be

$$\begin{pmatrix} 0.998 & -0.032 & -0.032 \\ -0.032 & 0.001 & 0.001 \\ -0.032 & 0.001 & 0.001 \end{pmatrix} \cdot K^\alpha, \quad \begin{pmatrix} 0.983 & -0.092 & -0.092 \\ -0.092 & 0.009 & 0.009 \\ -0.092 & 0.009 & 0.009 \end{pmatrix} \cdot K^\alpha. \quad (\text{S8})$$

In the orthogonal $\{\alpha'\beta'\gamma'\}$ basis, the general Heisenberg-Kitaev Hamiltonian can be expressed as:

$$\begin{aligned} H = & - \sum_{i<j} \tilde{J}_{ij} \mathbf{S}_i \cdot \mathbf{S}_j - \sum_{\langle i,j \rangle_\nu} \tilde{K}^\nu S_i^\nu S_j^\nu - \sum_{\langle i,j \rangle_{\mu\nu}} \Gamma_1 (S_i^\mu S_j^\nu + S_i^\nu S_j^\mu) \\ & - \sum_{\langle i,j \rangle_{\lambda\mu\nu}} \Gamma_2 (S_i^\lambda S_j^\mu + S_i^\mu S_j^\lambda + S_i^\lambda S_j^\nu + S_i^\nu S_j^\lambda) - A_{zz} \sum_i (S_i^z)^2, \end{aligned} \quad (\text{S9})$$

where $\Gamma_1 = \frac{B^2}{C^2}K$, $\Gamma_2 = \frac{AB}{C^2}K$, $\tilde{K}^\nu = \frac{(A^2-B^2)}{C^2}K$ and $\tilde{J}_{ij} = J_{ij} + \frac{B^2}{C^2}K$ for the nearest-neighbor exchange interactions, $\tilde{J}_{ij} = J_{ij}$ for others, and (λ, μ, ν) is any permutation of orthogonal basis vector's indexes $(\alpha', \beta', \gamma')$.

Although the non-zero off-diagonal terms in the matrix looks small, but here they will create an quite large negative component (e.g. CrSiTe₃: -0.7 meV, CrGeTe₃: -5.7meV) on the magnon gap at the Brillouin center and make the energy eigenvalues become imaginary unless an extra considerable anisotropy can be introduced to cancel it out. If so, either the anisotropy of the exchange interaction or the single ion anisotropy should be very strong. However, as we known from the magnetization and the critical behavior, the magnetic anisotropy in CrXTe₃ is quite small actually. Even if the magnon dispersion can be reproduced very well when the bond-dependent Kitaev interactions are assumed to be perfectly orthogonal, it is still difficult to understand the huge difference of the strength of the Kitaev interaction between CrSiTe₃ and CrGeTe₃, since the Kitaev interaction mainly arise from the heavy ligands (namely, Te of CrXTe₃) (57, 59). We can not completely exclude the existence of the Kitaev interaction, but

comparing to the previous DM model, the Heisenberg-Kitaev model is unlikely a proper model to describe the exchange interactions in this system at least.

3 Magnon band topology

3.1 Berry curvature and Chern number

Formulating semiclassical equations of motion for magnon wave packets (60), which include the anomalous velocity leads to a non-zero Berry curvature. We generally define the Berry curvature field associated with the n^{th} magnon band as

$$\Omega_{n\mathbf{k}} = i \sum_{m \neq n} \frac{\langle \Psi_{n\mathbf{k}} | \partial_{\mathbf{k}} H(\mathbf{k}) | \Psi_{m\mathbf{k}} \rangle \times \langle \Psi_{m\mathbf{k}} | \partial_{\mathbf{k}} H(\mathbf{k}) | \Psi_{n\mathbf{k}} \rangle}{(\epsilon_{n\mathbf{k}} - \epsilon_{m\mathbf{k}})^2}, \quad (\text{S10})$$

where $\partial_{\mathbf{k}} H(\mathbf{k})$ denotes the gradient of the Hamiltonian in momentum space. $\epsilon_{m\mathbf{k}}$ and $\epsilon_{n\mathbf{k}}$ are the magnonic eigenvalues.

Based on this Berry curvature, we can classify the topology of the n^{th} magnon branch using Chern number:

$$C(P) = \frac{1}{2\pi} \int_P \Omega(\mathbf{k}) \cdot \tilde{\mathbf{n}} dP, \quad (\text{S11})$$

where P is a two-dimensional slice of the BZ and $\tilde{\mathbf{n}}$ is its normal vector. In our calculation, the $\tilde{\mathbf{n}}$ is selected perpendicular to the xy plane. As the lowest three branches cross with each other, the lower three branches are sum together.

	J_{ab1}	J_{ab2}	J_{c1}	J_{c2}	K
CrSiTe ₃	0.4	0.2	0.08	0.065	3
CrGeTe ₃	0.24	0.42	0.1	0.08	6.5

Table S1: The parameters of the Heisenberg exchange interactions and the Kitaev interactions are listed together for CrSiTe₃ and CrGeTe₃. The local $\{\alpha\beta\gamma\}$ basis is assumed perfectly orthogonal and the single-ion anisotropy is fixed to 0.01 meV. The unit of the parameters is meV.

The Berry curvature distribution of bulk CrGeTe₃ in the first BZ is shown in Fig.S9(a,b). The Chern number of the lowest three branches is -3 and the Chern number of the highest three branches is $+3$. If we ignore the interlayer interaction, we can easily use the monolayer system to characterize the topological properties of the system, and the corresponding Berry curvature is shown in Fig.S9(c,d) with the Chern number -1 for the lowest branches. From the figure, almost the same Berry curvature distribution can be obtained. Compared to the intralayer interaction, the interlayer interaction is weaker and the DM interaction only exist among intralayer. In CrXTe₃, each layer contributes one optical and acoustic branches. The interlayer interaction splits the three degenerate bands but influence little on their topological properties.

3.2 Edge states and thermal Hall conductivity

To simplify the calculation, the monolayer CrXTe₃ is utilized to study the edge states. Here, the color scale of the bands in the main text Fig.4 is calculated based on the following equation:

$$LW(\mathbf{k}, j) = \sum_i \phi^{i*}(\mathbf{k}, j) \phi^i(\mathbf{k}, j) (R_z^i - 0.5), \quad (\text{S12})$$

where \mathbf{k} is the reciprocal space vector, j denotes the band index, i numbers the magnetic atom, and R_z^i represents the normalized position for atom i along the z -axis. $\phi^i(k, j)$ is the components of the right eigenstates of j at the magnetic atom i .

Given the nontrivial topology, the topological magnon edge states can contribute to the transverse thermal Hall voltage under an applied longitudinal temperature gradient (18, 24–26, 60), namely the topological thermal Hall effect.

The energy-dependent contribution to the ij 'th Cartesian component of the thermal Hall conductivity tensor $\hat{\kappa}$ can be calculated as

$$\kappa^{ij}(\epsilon) = \frac{k_B^2 T}{(2\pi)^3 \hbar} \sum_n \int_{\text{BZ}} \delta(\epsilon_{n\mathbf{k}} - \epsilon) C_2(f_n^B) \Omega_n^{ij}(\mathbf{k}) d\mathbf{k}, \quad (\text{S13})$$

where n enumerates the magnon bands, f_n^B is the Bose-Einstein distribution function, which can be expressed as $f_n^B = (e^{\epsilon_{n\mathbf{k}}/k_B T} - 1)^{-1}$, and C_2 is given by

$$C_2(x) = (1+x) \left(\ln \frac{1+x}{x} \right)^2 - \ln^2 x - 2\text{Li}_2(-x), \quad (\text{S14})$$

with Li_2 denoting the dilogarithm function. In our calculation, only the result of transverse thermal Hall conductivity κ^{xy} is shown, as the κ^{xz} and κ^{yz} is zero. The transverse thermal Hall conductivity of the system is then defined as $\kappa^{xy} = \lim_{\mu \rightarrow \infty} \kappa_{\mu}^{xy}$, where $\kappa_{\mu}^{xy} = \int_0^{\mu} \kappa^{xy}(\epsilon) d\epsilon$ is the cumulative thermal Hall conductivity.

From the experimental results, we know that the respective Curie temperature of CrSiTe_3 and CrGeTe_3 are around 30 K and 60 K. The calculated temperature-dependent and energy-dependent thermal Hall conductivity are shown in Fig.S11. For both materials, κ^{xy} is significant enhancement in the energy region close to the band gap, which can be attributed to the distribution of the Berry curvature around the K point. In low temperature only these "topologically-trivial" states are excited according to the Bose-Einstein distribution, leading to the zero platform at very low temperature. Then conductivity increases as the temperature increases. The effect of the DM interaction is shown in Fig.S11(e), from which we can observe that the thermal Hall conductivity increases with the enhancement of the DM Interaction.

The predicted thermal Hall conductivity for CrGeTe_3 reaches the order of 10^{-4} W/Km, which is large enough to be observed in experiment. Furthermore, the DM interaction value is determined by the strength of spin-orbit coupling. Compared to CrGeTe_3 and CrSiTe_3 , CrSnTe_3 and CrPbTe_3 should have even stronger spin-orbit coupling and some recent theoretical studies have demonstrated that the corresponding monolayer system could have a ferromagnetic state with higher Curie temperatures (47, 48). These materials are thus more likely to have even

bigger thermal Hall conductivity than $\text{Lu}_2\text{V}_2\text{O}_7$ (23, 24).

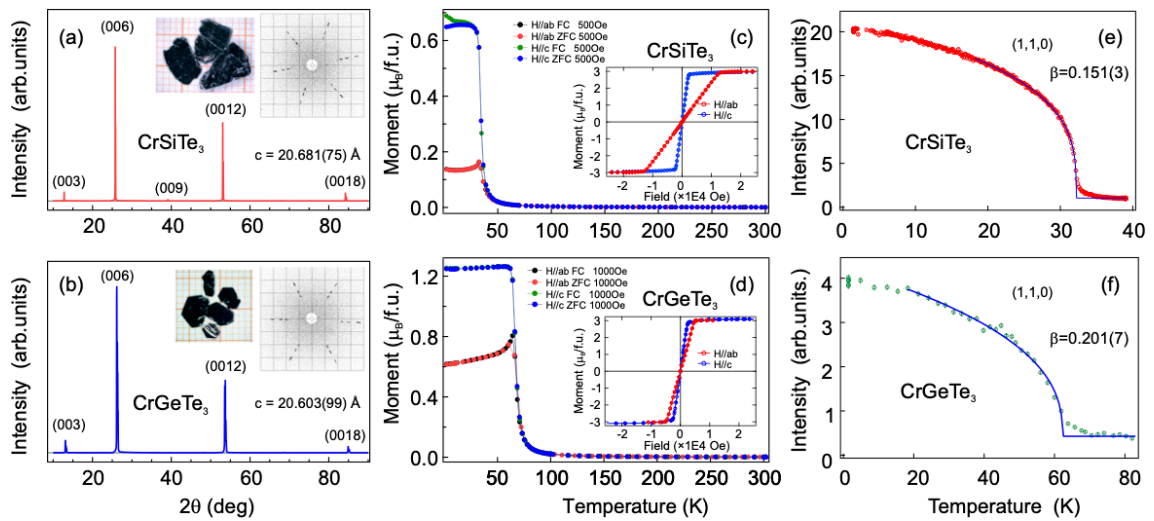


Figure S1: **X-ray diffraction and magnetic properties of CrXTe₃.** (a,b) X-ray diffraction of single-crystal CrSiTe₃ and CrGeTe₃ at 300 K. The insets are the sample pictures and the corresponding X-ray Laue pattern of the (H,K,0) reciprocal plane. (c,d) ZFC/FC magnetization curves measured under applied magnetic fields along the *c* and *a* axes. Insets show the corresponding magnetization as a function of field at 2 K for *H* || *c* and *H* || *ab*. (e,f) Temperature dependence of the (1,1,0) magnetic Bragg peak intensity of CrSiTe₃ and CrGeTe₃ measured at DNS, MLZ. The solid lines are the fittings of the experimental data in the vicinity of the ferromagnetic transition. Photo Credit: Fengfeng Zhu, Forschungszentrum Jülich.

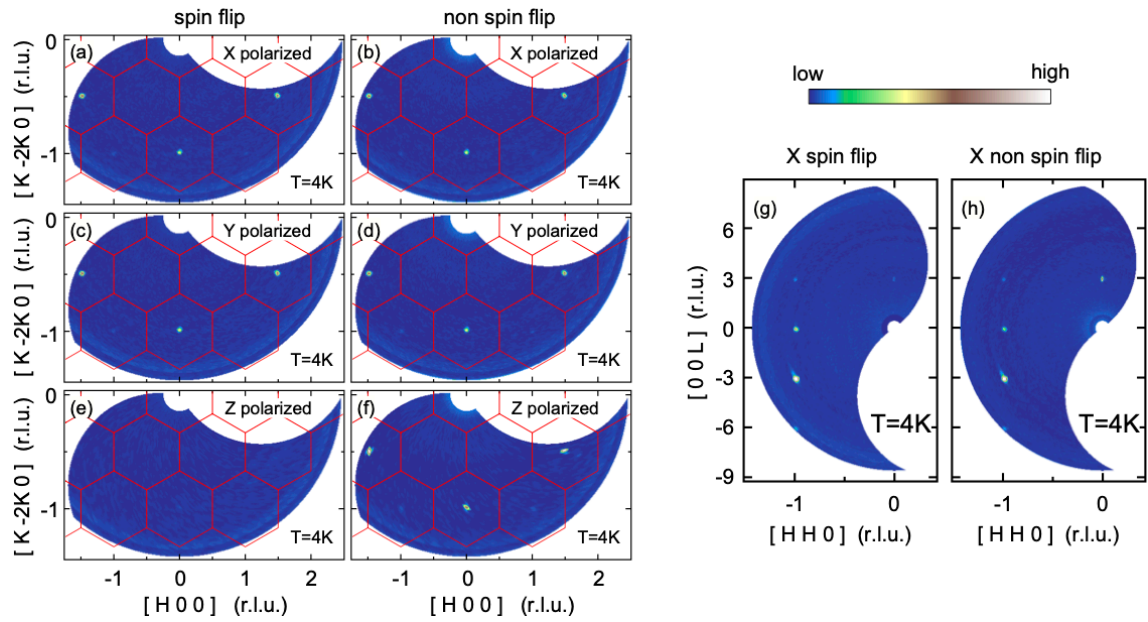


Figure S2: **Polarized elastic neutron scattering maps.** (a-f) Q Maps in the $(H, K, 0)$ scattering plane and (g,h) in the (H, H, L) scattering plane measured on CrGeTe_3 at DNS. Red solid lines are the Brillouin zone boundaries.

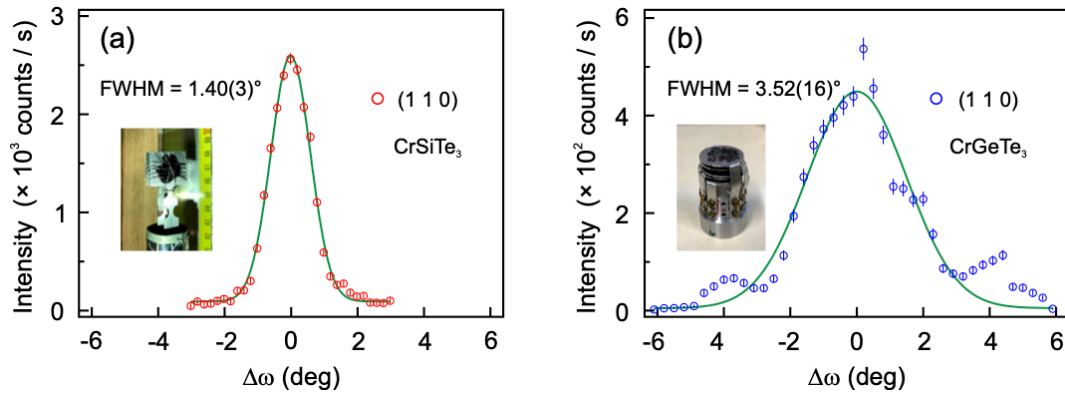


Figure S3: **Mosaic width of the co-aligned CrXTe_3 samples.** (a),(b) Rocking curve scans of the $(1, 1, 0)$ nuclear reflection at about 80 K show the alignment quality of CrSiTe_3 (with 2 pieces) and CrGeTe_3 (with more than 100 pieces) respectively. The insets are the corresponding pictures of the samples measured at IN8. Photo Credit: Fengfeng Zhu, Forschungszentrum Jülich.

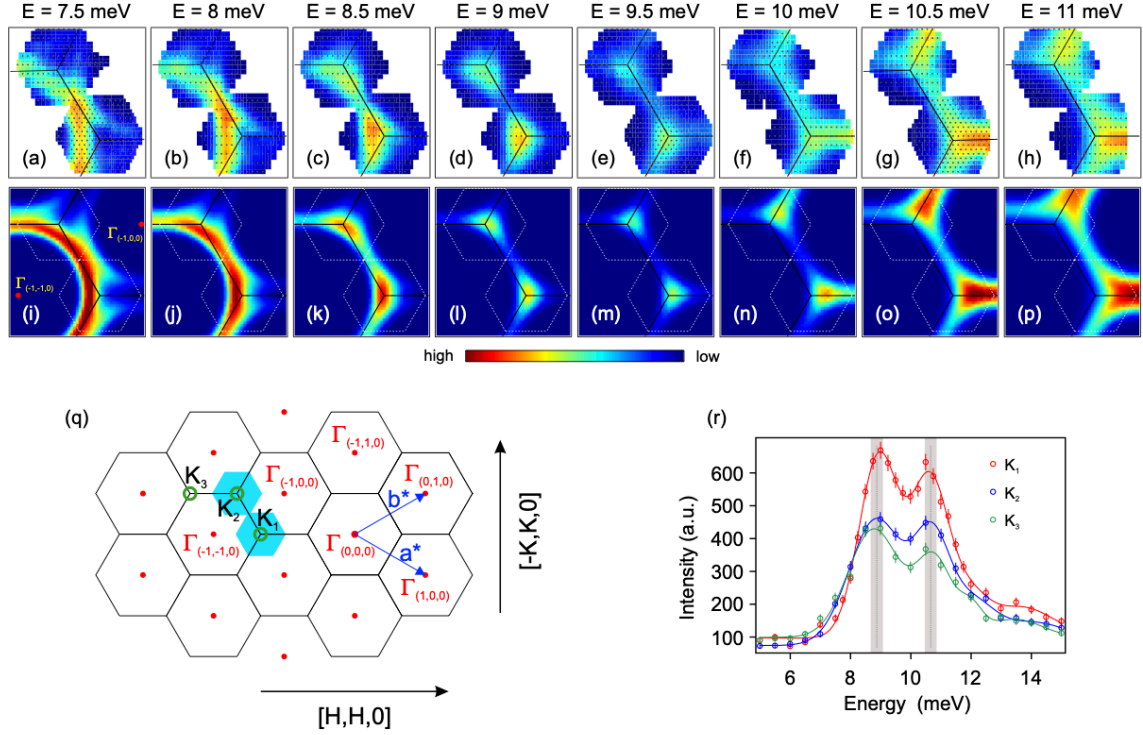


Figure S4: **Spin-wave excitations of CrSiTe₃ in the (H,K,0) scattering plane.** (a-h) Constant-energy mappings of the magnon spectra of CrSiTe₃ in the (H,K,0) scattering plane measured at the thermal neutron triple-axis spectrometer PUMA. The energies of the constant-energy mappings are chosen to cover the whole energy scale of the opened gaps at the K points with an energy step of 0.5 meV. The black solid lines denote the boundaries of the 2D BZs. The dark gray dots represent the actually measured Q points. (i-p) Calculated constant-energy mappings using the parameters of the 2nd-NN DM interaction model in this paper. The calculated spectra are convolved with the estimated instrument energy resolution of 1.5 meV. Areas inside the white dashed lines corresponds to the Q range for the experimental data. (q) Schematics of the projected 2D BZs. The BZ center Γ points and 3 selected K points are denoted by the red dots and green circles, respectively. The light blue hexagon is a schematic for the corresponding Q positions for the experimental data in (a-h). (r) Constant- Q energy scans of the magnon spectra at 3 different K points in (q). The solid lines are the multi-peak Gauss fitting. The dash lines and grey shadow represent the averaged energy positions and error bars for the magnon bands at the K points.

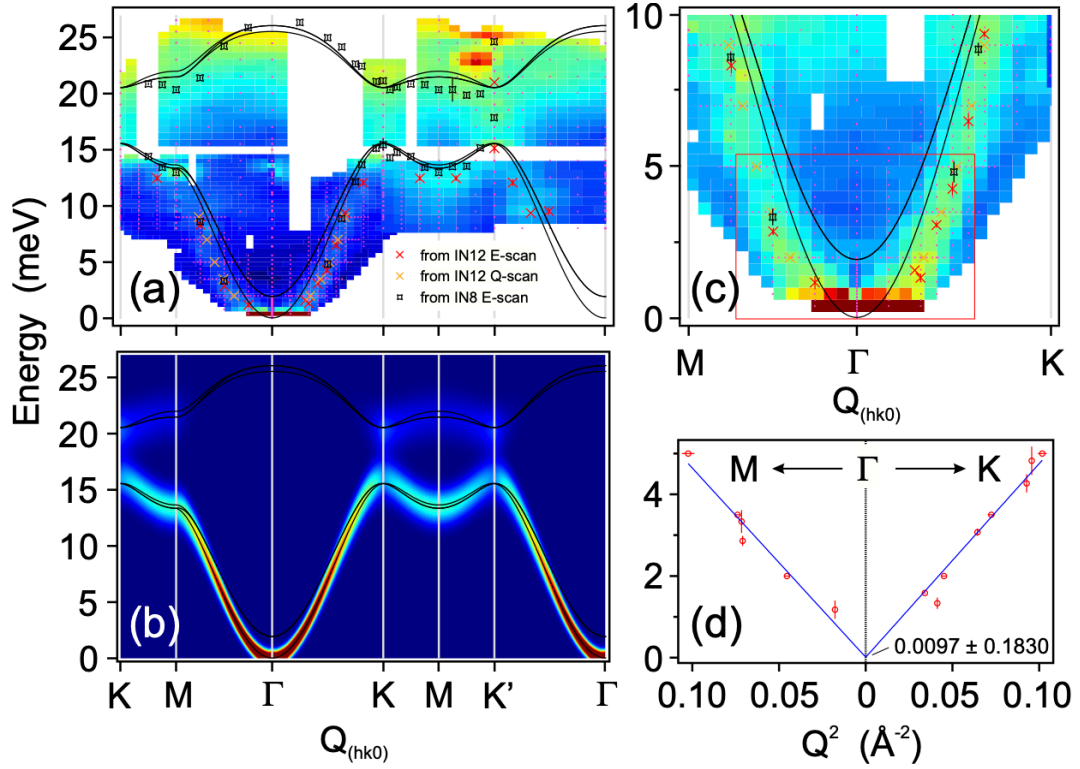


Figure S5: **The low-energy magnon branches of CrGeTe₃.** (a) The magnon spectra of CrGeTe₃ measured at the cold neutron triple-axis spectrometer IN12 (with a fixed $k_f = 1.7 \text{ \AA}^{-1}$ and 2.8 \AA^{-1}). The solid lines are the calculated magnon dispersion curves. The isolated crosses and stars are the fitted peak positions of various constant- Q and constant- E scans. (b) The corresponding calculated magnon spectra by using the 2nd-NN DM interaction model. (c) Enlarged plot of the low energy excitations in (a). (d) Quadratic fitting of the magnon band for the low energy parts. Only the peak positions inside the red rectangle in (c) are included in the fitting.

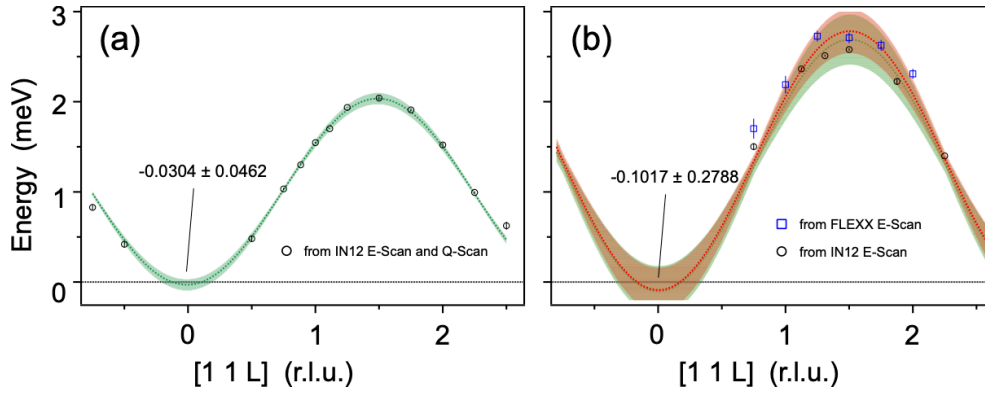


Figure S6: **Fitting of the magnon dispersion along the [1,1,L] direction.** (a),(b) Cosine-function curve fittings of the respective magnon band dispersion of CrSiTe_3 and CrGeTe_3 along the [1,1,L] direction. The green dashed lines in (a,b) are the fittings according to the data collected from IN12 ($k_f = 1.7 \text{ \AA}^{-1}$). The red dashed line in (b) is a combined fittings with the restriction in Fig.S5(d) according to all the data of CrGeTe_3 collected from IN12 and FLEXX. The light shading zones represent the confidence interval with a width of 2 standard errors.

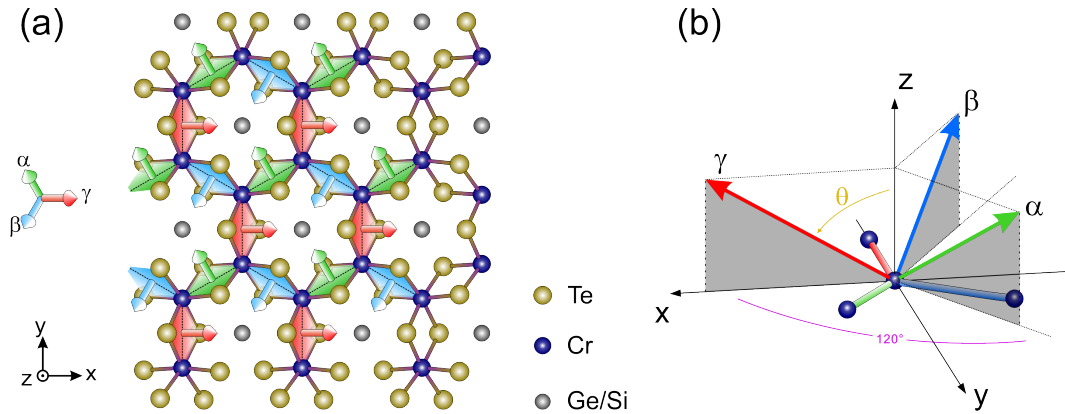


Figure S7: **The proposed Kitaev model for CrXTe_3 .** (a) Schematic plot for the Kitaev model. The red, blue and green rhombus planes marked with perpendicular arrows are almost orthogonal to each other, which are used to represent 3 different bonds of the Kitaev model. (b) The configuration of the local $\{\alpha\beta\gamma\}$ coordinate in the global $\{xyz\}$ coordinate.

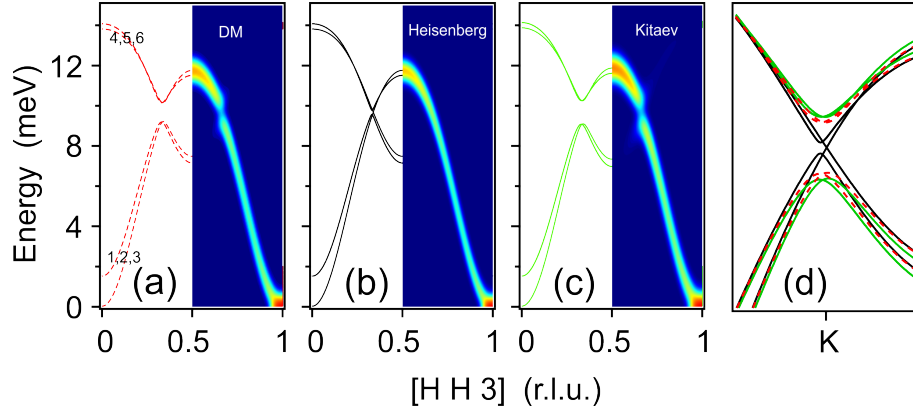


Figure S8: **Comparison of the calculated magnon spectra with different models.** (a) Magnon spectra calculated by using the Heisenberg with 2nd-NN DM interaction model. Dash lines are the calculated magnon spectra at the BZ boundaries, and the intensity maps are the convoluted results with energy resolution of 1 meV. (b) Magnon spectra calculated by using a simple Heisenberg model. (c) Magnon spectra calculated by using the Heisenberg with a modified Kitaev interaction model. (d) Comparison of the magnon band dispersion near the Dirac point between all the models in (a-c).

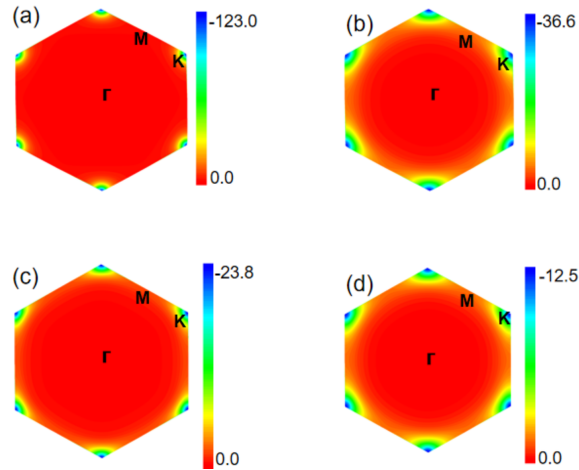


Figure S9: **The calculated Berry curvature in the $K_x - K_y$ plane.** The Berry curvature for the lowest three magnon branches of bulk CrSiTe_3 (a) and CrGeTe_3 (b). The Berry curvature for the lowest branch of monolayer CrSiTe_3 (c) and CrGeTe_3 (d) in the first Brillouin zone. The Chern number is -3 for (a,b) and -1 for (c,d).

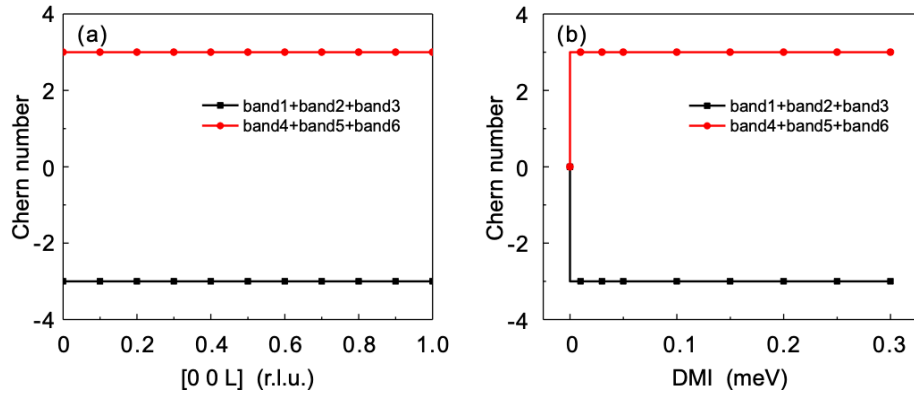


Figure S10: **Chern numbers of magnon bands.** (a) The Chern number along the [0,0,L] direction. The sum of the Chern numbers are -3 and 3 for the lowest and highest three bands respectively. (b) The influence of the magnitude of the DM interaction on the Chern numbers of the bands.

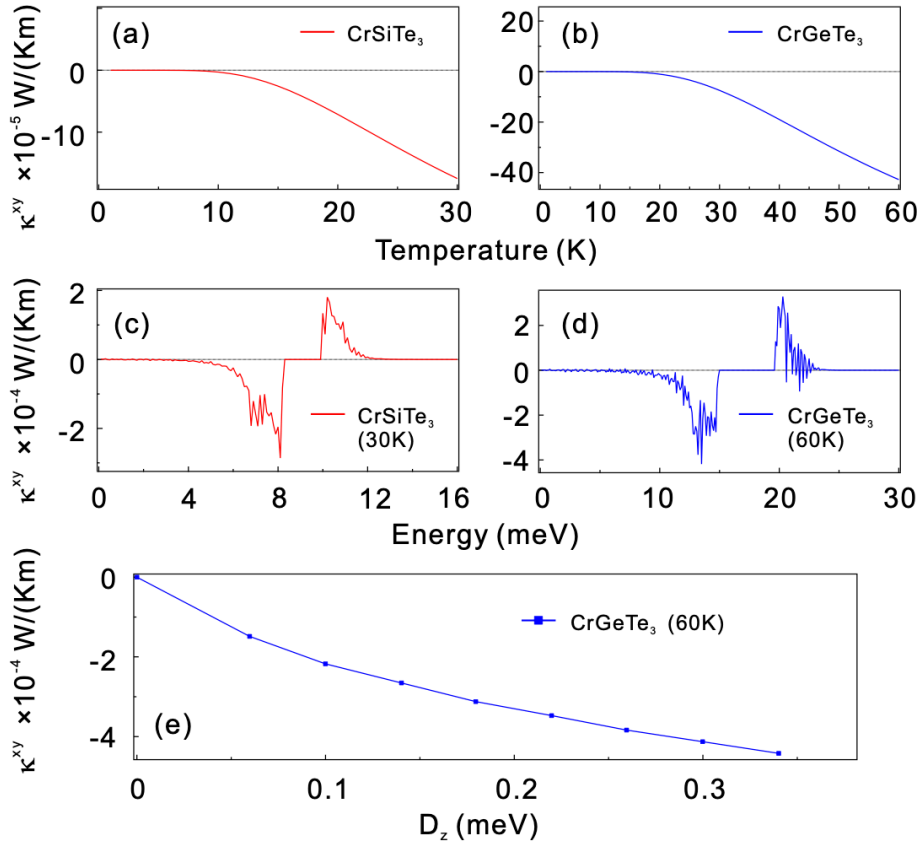


Figure S11: **The calculated transverse thermal Hall conductivity (κ^{xy}) of CrGeTe₃ and CrSiTe₃.** The temperature dependence (a, b) and energy dependence (c, d) of the thermal Hall conductivity of CrGeTe₃ and CrSiTe₃. The κ^{xy} with the function of D_z for CrGeTe₃ at 60K is shown in (e).